

# Polydisperse Solid Foams: Multiscale Modeling and Simulations of Elasto-Acoustic Properties Including Thin Membrane Effects

C. T. Nguyen<sup>a,b</sup>, V. Langlois<sup>c</sup>, J. Guilleminot<sup>d</sup>, F. Detrez<sup>a</sup>, A. Duval<sup>b</sup>, M. Bornert<sup>e</sup>, P. Aïmedieu<sup>e</sup>, C. Perrot<sup>a,\*</sup>

<sup>a</sup>MSME, Univ Gustave Eiffel, CNRS UMR 8208, Univ Paris Est Creteil, F-77454 Marne-la-Vallée, France

<sup>b</sup>Trèves products, services and innovation, 2-4 rue Emile Arquès, CS 70017, 51686 Reims Cedex 2, France

<sup>c</sup>Navier, Univ Gustave Eiffel, ENPC, CNRS, F-77447 Marne-la-Vallée, France

<sup>d</sup>Department of Civil and Environmental Engineering, Pratt School of Engineering, Duke University, P.O. Box 90287, 121 Hudson Hall, Durham, North Carolina 27708-0287, USA

<sup>e</sup>Navier, Univ Gustave Eiffel, ENPC, CNRS, IFSTTAR, F-77447 Marne-la-Vallée, France

---

## Abstract

This work is concerned with the prediction of the elasto-acoustic properties of polydisperse solid foam structures. A highly polydisperse foam sample is first characterized using microtomography and scanning electron microscopy. Relevant geometrical properties are then determined by image processing and utilized to model the partially closed cell system with random Laguerre tessellations. The macroscopic visco-thermal transport properties of the solid foams are next calculated by numerical techniques, using either finite element computations or pore-network simulations. The permeability and sound absorption coefficient at normal incidence are also measured and a good agreement is obtained with the calculations when the elasto-acoustic coupling is modeled from the Biot's equations (including characterized visco-elastic parameters). Our results demonstrate that stochastic geometry provides a robust framework to understand the structure-property relationships of polydisperse foam.

*Keywords:* Polydisperse foam, Microtomography, Microstructure reconstruction, Transport parameters, Elasto-acoustic properties.

---

## 1. Introduction

Understanding the physical mechanisms controlling the macroscopic properties of a disordered [1, 2] and locally inhomogeneous [3] foam is an open fundamental issue in material sciences [4, 5, 6, 7]. The random structures of inhomogeneous solid foams such as polyurethane are very similar to those of their three-dimensional polycrystal counterparts. The random nature of the pore size and asphericity distributions produce heterogeneity at the local scale. In such systems, it has been argued that an appropriate polyhedral description consistent with experimental data of the microstructure can be obtained with optimal Laguerre tessellations [8]. However, to describe the passage from the local geometry of the disordered media to the macroscopic properties of interest, solving the local partial differential equations which govern the phenomena needs to be explicitly addressed [9, 10]. So far, this resolution has been limited to idealization of the local geometry through regular polyhedrons [11, 12]. Another fruitful path has been the development of analytical methods such as the self-consistent models [13, 14], or the determination of bounds based on the use of moments of the pore space distribution [9]. These general approaches are useful to find rapid

approximate solutions of the problem, but cannot be considered when an accurate estimate is required for random structure exhibiting a wide distribution of pore sizes.

When a foam is loaded with solid particles during the foaming process, it is commonly observed that the final foam density and cellular structure are affected [15], with coexisting small and large cell sizes in the vicinity of the solid particle. This microstructural modification, sometimes referred to as nucleation effects, differs from free-rise foaming process, in which homogeneity occurs from the competing reactions between foam expansion and cellular structure stabilization. The change in cell size distribution is likely to be accompanied by a modification of the other geometric characteristics, such as number of face per cell and number of edges per face [16] or membrane content [17]. Random foams with a wide range of cell-volume distributions are also observed when real foam materials evolve through diffusive coarsening [18, 19, 20, 21].

The aim of the present study is to propose and validate a pipeline integrating fine-scale experiments and computational simulations to predict the acoustics properties of realistic, polydisperse foams. In contrast to the study presented in Ref. [11] where computational homogenization is applied on a simplified model involving two types of Kelvin cells (the properties of which are identified based on microstructural data), the methodology advanced in

---

\*Corresponding author

Email addresses: cong-truc.nguyen@univ-eiffel.fr (C. T. Nguyen), camille.perrot@univ-eiffel.fr (C. Perrot)

this paper accounts for a more complete statistical description of the underlying microstructure—hence allowing for the influence of polydispersity and membrane content to be systematically quantified. Numerical homogenization methods [22], combined with semi-phenomenological models [23, 24], offer the ability to study how volume-averaged properties of the flow relate to microscopic details of the geometry. A two-step methodology is followed that involves microstructure reconstruction and solving local partial differential equations. However, the passage from idealization of the local geometry to a more realistic disordered one has been limited due to the prohibitive calculation time associated with the resolution of boundary value problems corresponding to large spatial domains [25]. This motivates the use of a pore-network approach [26, 27] for the case of the viscous fluid flow. The use of this method and finite element simulations (to solve the potential flow and heat conduction equations) allows us to reproduce many features of microscopically-disordered foams and to determine the corresponding transport properties. This enables, in particular, the consideration of locally heterogeneous foams with about five hundred pores, as well as the exploration of results sensitivity with respect to the solid film or membrane content (for given pore size and sphericity distributions). In addition, the framework accounts for elasto-acoustic effects by integrating the elastic properties of the studied foam sample. The foam sample used for microstructure characterization contains about two thousand pores characterized using tomography, which is large enough to observe and describe the polydispersity and its effect on the transport and sound absorbing properties. In order to be statistically representative, the analyzed volume must contain a sufficiently large number of heterogeneities. In practice, the characteristic size of the domain can be assessed through a convergence analysis on statistical metrics and is typically found to be about ten times larger than the characteristic size of the heterogeneities [28, 29, 30, 31].

This paper is organized as follows. The geometrical properties of the studied polyurethane foam sample are presented in Section 2, together with the calculation method of the macroscopic properties. Section 3 is devoted to a comparison between multi-scale computations and experimental measurements. Finally, some concluding remarks are provided in Section 4.

## 2. Microstructure and Properties

In this work, we consider a polyurethane (PU) foam obtained by adding graphite particles during processing. Such particles are commonly introduced during the foaming process to improve fire resistance [32, 33, 34, 35, 36, 37], and were reported to modify the distribution of pore size and to increase the heterogeneity in the PU foam [38, 39].

### 2.1. Characterization of Polydispersity and Membrane Content

The microstructure of the foam is characterized using both X-ray computed tomography (X-ray CT) and Scanning Electron Microscope (SEM) images. The former technique is specifically used for the characterization of pore size, sphericity, and number of neighbors; while membrane properties are studied based on SEM images.

#### 2.1.1. Pore Characterization

A X-ray micro computed-tomography ( $\mu$ CT) local tomography was performed using an UltraTom microtomograph from RX-Solutions, which includes a Hamamatsu micro-focus 230 [kV] model L10801 X-Ray source and a CsI scintillator Varex flat-panel imager model 4343 DX4, which total number of active pixels is  $3052 \times 3052$ . A parallelepipedical sample (approx.  $11 \times 11 \times 23$  [mm<sup>3</sup>]) of PU foam was cut. Acquisition was conducted with tube voltage and current set to 60 [kV] and 100 [ $\mu$ A], respectively. Imager parameters were: 1 frame per second averaged on 32 images using a  $2 \times 2$  binning. Voxel size was 6 microns, and the size of the reconstructed volume was  $7.8 \times 7.8 \times 7.8$  [mm<sup>3</sup>].

The use of adapted filters and a binarization are required to reconstruct the struts in foam CT images. Details regarding image processing for the PU foams are provided below.

1. First, noise reduction is performed by extracting a subdomain of  $1000 \times 1000 \times 1000$  voxels at the center of the domain (containing  $1300 \times 1300 \times 1300$  voxels), to reduce lateral noise reconstruction artifacts. A ball-shaped dilatation filter with a radius of 2 voxels is then applied to compensate for artificially disconnected solid skeleton (lack of resolution) Fig. 1a.
2. Second, foam struts are obtained through a binarization, by applying Otsu’s method [40] with an adapted threshold (which is calculated for each slice), Fig. 1b.
3. Third, a 3D distance transform map is computed and used to proceed with image inversion; Fig. 1c.
4. Last, a segmentation by watershed transform is performed to detect the borders separating one pore from the others [41, 16], and the pores thus detected are colored, Fig. 1d.

The general workflow for image analysis is illustrated in Fig. 1. In this work, the solid particles were considered in the image processing sequence as solid walls that separate neighboring pores. No attempt was made to explicitly identify them and model their role. An influence of graphite particles on the foam structure can however be observed in panels e) and f). Specifically, small pores are created around the graphite particles that contribute to

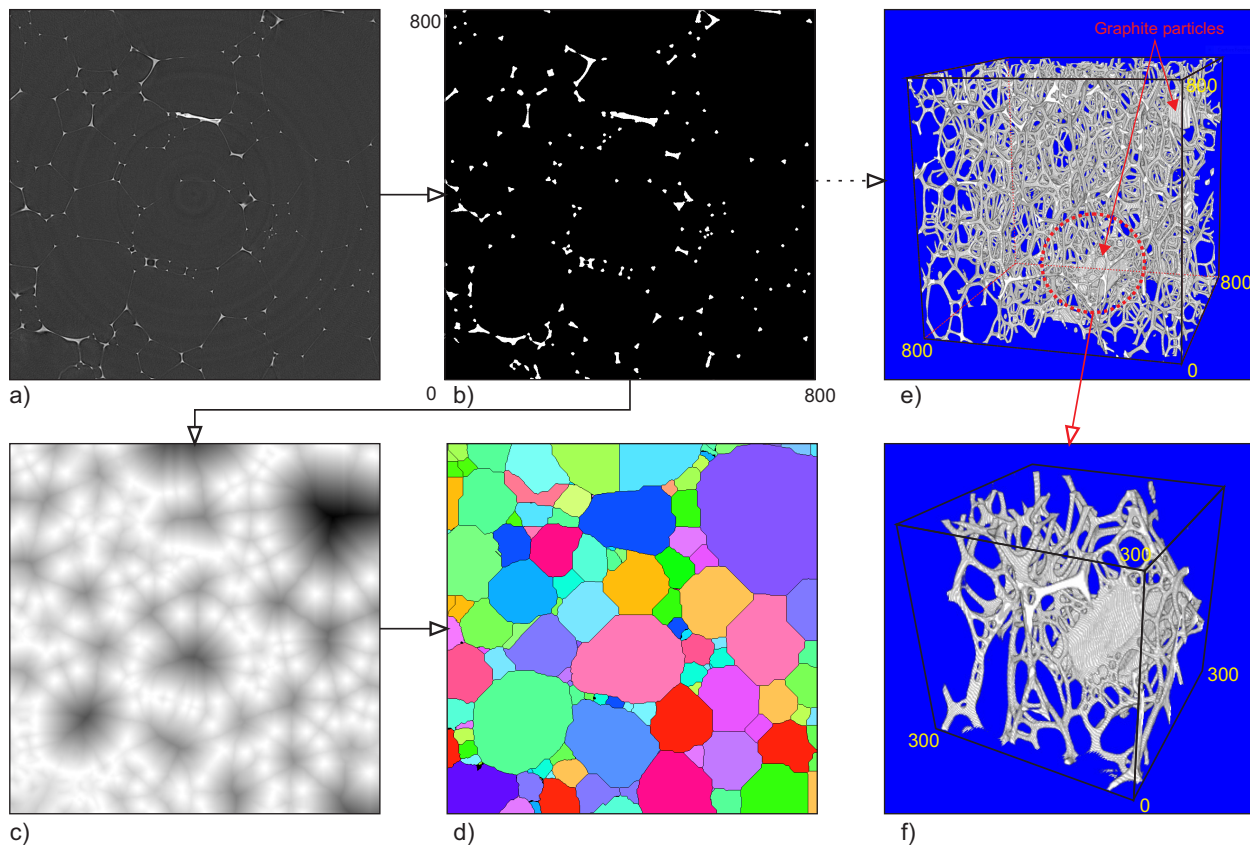


Figure 1: (Color online) General workflow for image analysis: a) original CT image; b) binarized image generating the struts system of foam; c) image obtained after distance transform and inversion; d) pores detected through a segmentation with a watershed transform; e-f) 3D visualization of the struts system and graphite particles.

the rigid skeleton. Here, a volume of  $6 \times 6 \times 6$  [mm<sup>3</sup>] containing 2,131 pores was analyzed.

Once the images have been processed, several morphological characteristics, including the volume and surface of pores and spatial arrangement properties (such as relative positions and numbers of neighboring pores), can be extracted. Notice that only complete pores are accounted for to estimate the pore size distribution (in other words, pores intersecting image borders and solid particles are discarded) in the present analysis. On the other hand, pores located at the borders were preserved to estimate the number of neighbors. All image processing and analysis steps were carried out by using the open-source FIJI software with the MorphoLibJ plugins [42, 43].

Two parameters can be used to characterize the pore size and shape (as compared to a sphere). The pore size is defined by an equivalent diameter  $d$ , which represents the diameter of a sphere with a volume equal to the pore volume, denoted by  $V_p$ . The pore shape is measured by the sphericity  $s$ , which is defined as the ratio of the surface area of a sphere having the same volume as the pore over the surface area  $S_p$  of the pore:

$$s = \frac{(36\pi)^{1/3} V_p^{2/3}}{S_p}. \quad (1)$$

Notice that the maximum  $s = 1$  is obtained for a spherical pore. For examples, Voronoi tessellations provide sphericities exhibiting an average of 0.810 and a standard deviation of 0.044 [8]. The mean values and standard deviations for  $d$  and  $s$ , estimated from the data, are provided in Tab. 1.

### 2.1.2. Membrane Characterization

The characterization of membranes is performed by analyzing the surfaces of foam samples with SEM images. Scanning electron microscopy is based on the detection of secondary electrons emerging from the surface under the impact of a very fine brush of primary electrons (sweeping across the observed surface). It therefore requires electrically conductive materials. For non-conductive materials, a metallization of the samples is needed. A high performance metallizer by cathode sputtering, coupled with a magnetron source (Cressington sputter coater 208HR), makes it possible to deposit a conductive film of a few nanometers (controlled by a quartz probe, here a Cressington MTM 20) on the surface of the samples. Fig. 2(a) shows a large contrast between the largest and the smallest cells. A close-up of a solid film or membrane covering most of the windows is displayed in Fig. 2(b). In the vicinity of a graphite particle, a large number of small windows can

be seen, suggesting a nucleation effect (leading locally to smaller window sizes), Fig. 2(c). We examined the foam structure including closed and open windows, to further characterize the foam structure, Fig. 2(d).

In this work, a polygon is superimposed over each individual window in the images thus obtained. For each open membrane, another polygon is used to characterize the area of the corresponding aperture size; see Fig. 2(d). The area of the superimposed polygons is then determined. The proportions of closed ( $x_c$ ) and open ( $x_o$ ) membranes, defined as the ratios between the number of closed or open membranes (denoted by  $N_{cl}$  and  $N_{op}$ , respectively) and the total number of membranes  $N_{total}$ , are also identified. The aperture ratio of open membranes is estimated as  $t_o = \sqrt{A_{ap}/A_{ow}}$ , where  $A_{ow}$  is the area of the aperture corresponding to a window for which the membrane is open, and  $A_{ap}$  is the area of the polygon associated with the given window. Note that if a membrane has several apertures,  $A_{ap}$  is their total area. The average of aperture ratio  $\langle t_o \rangle$  is subsequently deduced. The number of edges per membrane  $N_e$  is also characterized. Due to sample cutting, some membranes may be destroyed or damaged, in which case they are discarded in the analysis. It is noteworthy that the apertures of open membranes are continuous and thus can be distinguished from destroyed membranes that are characterized by a geometry which is singular and consists of abrupt modifications at the periphery of the individual apertures (see the distinction between destroyed and open membranes in Fig. 2d).

For the PU foam under study, dozens of SEM images associated with both the top and bottom sample surfaces were analyzed, leading to the characterization of hundreds of membranes. The foam presents many fully-closed membranes. The mean value for the proportion of fully-closed membranes is  $\langle x_c \rangle = 0.72$ , and the average of aperture ratio for the open membranes is estimated to  $\langle t_o \rangle = 0.51$  (see Tab. 1).

$d$ ( $\mu\text{m}$ )	$s$ (-)	$\langle x_o \rangle$ (-)	$\langle t_o \rangle$ (-)
$360 \pm 290$	$0.77 \pm 0.068$	$0.28 \pm 0.05$	$0.51 \pm 0.17$

Table 1: Geometric properties of the PU foam.

The thickness of a membrane is also estimated through SEM images (see Fig. 2b). Its average value is around  $0.3$  [ $\mu\text{m}$ ], which is noticeably smaller than the values reported elsewhere for polyurethane foams [11, 12]. One can note that the membrane thickness is very thin when compared to the average pore size  $\langle d \rangle = 360$  [ $\mu\text{m}$ ]. This property justifies that the thickness of the membranes separating the cells is further ignored, assuming that we wish to reduce the size of a finite element model. Appendix A describes the implementation and the validation of the finite-element model used to compute the viscous characteristic length of polydisperse solid foams in which the solid wall thickness (membrane) is much smaller than the average pore size.

## 2.2. Polydisperse Microstructure Reconstruction

### 2.2.1. Methodology

Realistic foam microstructures usually exhibit a distribution of pore size. Random Laguerre tessellations are widely used to simulate polydisperse foams; see [44, 45, 16]. In these works, a Laguerre tessellation is constructed by using a random dense packing of hard spheres with a distribution of sphere size that coincides with the pore size distribution (estimated from the characterized foam samples). In classical Laguerre tessellation generation methods, large differences between the spherical and pore centroids may be observed; meaning that a quantitative reproduction of the pore size distribution estimated from experiments still remains a challenging task. In this work, we use an enhanced algorithm developed for the purpose of a description of 3D polycrystals [8]. The algorithm proceeds by sequentially updating the parameters of the seeds in the tessellation model, an optimization being performed through a genetic algorithm until some pore properties match with the target properties (prescribed distributions).

In order to proceed with the foam microstructure reconstruction, the pore size and the quantity  $1 - s$  related to pore sphericity are assumed to follow some suitable probability distributions, identified from the experiments. Note that periodic boundary conditions are used to avoid boundary effects and to increase the convergence rate with respect to domain size.

In the present work, we are primarily interested in highly porous and thin membrane-based foams. Specifically, membrane thickness and Plateau's borders are not modeled, which reduces the computational cost associated with subsequent finite element analyses. The membrane effects are accounted for through (1) the proportion of closed and open membranes ( $x_c$  and  $x_o$ ), and (2) the averaged aperture ratio  $\langle t_o \rangle$  of the open membranes. More specifically, a subset of  $x_o$  membranes is randomly selected amongst all membranes, and these membranes are opened using a polygon exhibiting the same aperture ratio  $\langle t_o \rangle$  (in practice, this defines a homothety with respect to the centroid of the membrane).

With a view towards finite element discretization, it is recommended to discard small faces (or membranes) in the opening procedure. In what follows, windows are ignored when the condition  $\lambda < \epsilon \langle \lambda \rangle$  is met, where  $\lambda$  is the window area,  $\langle \lambda \rangle$  is the average area, and  $\epsilon$  is a given threshold which is typically taken as  $0.01 \leq \epsilon \leq 0.10$  [46]; the applied value  $\epsilon = 0.05$  was used in this model. Fig. 3 shows a configuration of periodic geometry of 453 pores and corresponding mesh.

### 2.2.2. Comparison Between Real and Reconstructed Microstructure

In Fig. 4, we show the probability density functions of pore size and  $1 - s$  estimated (1) from the experimental data, (2) using log-normal models, and (3) after the

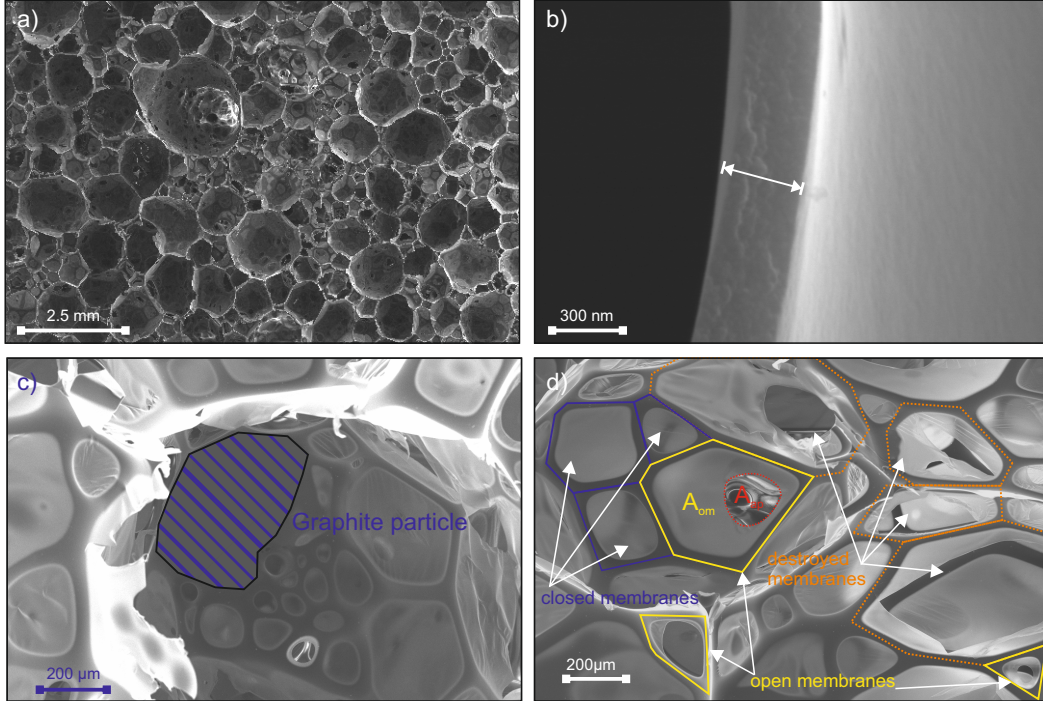


Figure 2: (Color online) Characterization of membranes on SEM images: (a) top view of foam sample; (b) membrane thickness; (c) graphite particle; (d) open membrane aperture ratio, and distinction between open and destroyed membranes.

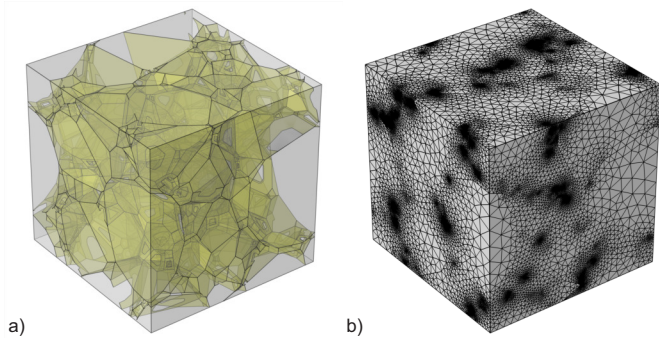


Figure 3: (Color online) A configuration of periodic geometry of 453 pores (a) and corresponding mesh (b).

microstructure reconstruction. The high value of the coefficient of variation for the pore size,  $CV_d = \sigma_d / \langle d \rangle = 0.79$  ( $\sigma_d$  denoting the standard deviation of the pore size  $d$ ), indicates a wide range of pore volumes. The lognormal fit for the pore size distribution is found in good agreement with the experimental results, which is consistent with other results provided elsewhere for cellular materials [44]. Similarly, the log-normal fit provides a fairly close approximation of the empirical function for the quantity  $1 - s$  (recall that  $s$  is the sphericity). It is seen that the experimental distributions for the pore diameter and sphericity are properly captured in the proposed methodology.

In order to further discuss model adequacy, results on various quantities of interest obtained through the experimental characterization and through the numerical recon-

struction (with 453 pores) are shown in Fig. 5. The number of neighboring pores in the reconstructed structure is  $N_v = 12.5 \pm 8.9$ , which is larger than the corresponding number  $N_v = 9.1 \pm 8.6$  in the physical foam. This discrepancy could be explained by a number of factors. First, the smallest windows were discarded for computational reasons (Sec. 2.2.1). Second, simulated pores are modeled as convex polyhedrons with straight struts, which represents a simplified geometrical description of the real foam structure (surface area minimization was not performed in this work). Third, the presence of graphite particles can affect the polyhedral microstructure of PU foams [47, 36], hence decreasing the number of neighboring pores. A small value for the number of neighboring pores could also be induced by the pore size distribution, as shown in [1, 16]. Indeed, the number of small cells increases with polydispersity and the small cells in polydisperse foams have fewer faces or neighbors (Fig. 3 of Ref. [1]). In agreement with simulations from the literature, our results also suggest that the number of neighboring pores and pore sizes are indeed correlated—small pores have fewer neighbors than larger ones, in both the experimental and simulated observations (Fig. 5b). On the other hand, the average number of edges per face for the simulated microstructure,  $5.07 \pm 1.39$ , is close to the value obtained on the experimental microstructure,  $5.07 \pm 1.31$  (see Fig. 5c).

These results support the relevance of the proposed methodology to sample microstructures of strongly polydisperse foams. We note that graphite particles modified the equilibrium microstructure of dry soap foams and led

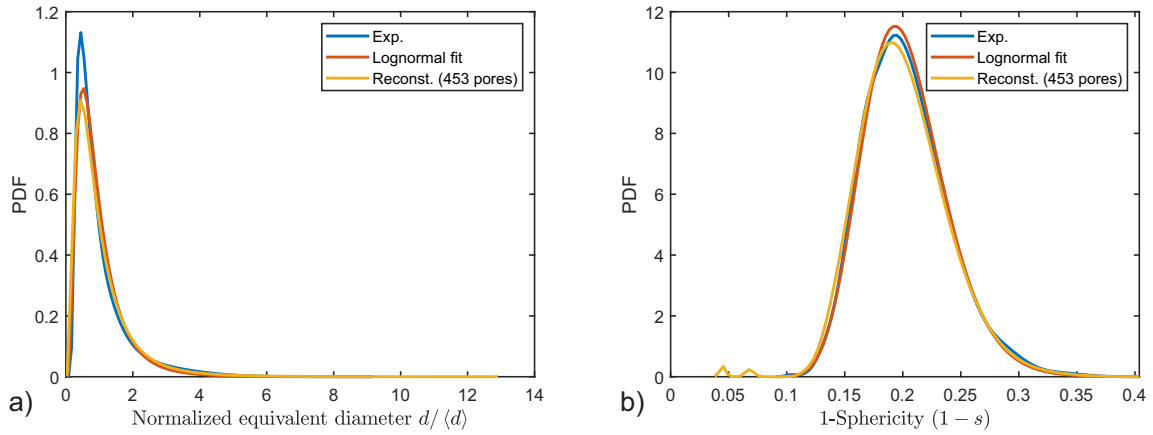


Figure 4: (Color online) Foam morphology comparison between experimental measure, fitted lognormal law and reconstruction for (a) pore size distribution and (b) 1-sphericity.

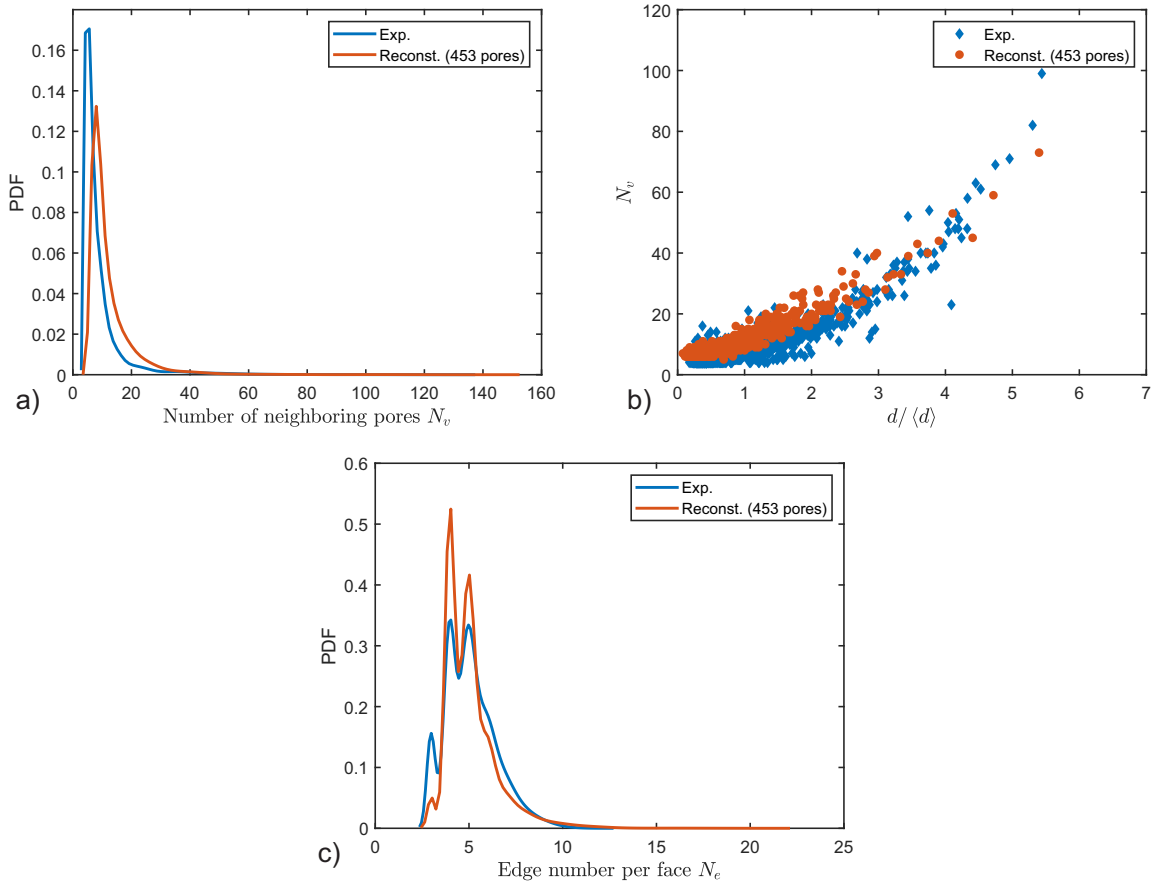


Figure 5: (Color online) Foam morphology comparison between experimental measure and reconstruction for (a) Number of neighbor, (b) Correlation between number of neighbor and normalized equivalent diameter and (c) Edge number per face.

to topological properties that are different from those reported in isotropic Plateau polyhedra. A promising research direction to further elucidate the mechanisms leading to non-universal topological and geometric properties of random foams including graphite particles would consist in using synchrotron X-ray nano-tomography to col-

lect the positions and shapes of graphite particles, and in performing a cross-correlation analysis involving some local topological descriptors. The ability of synchrotron tomography to provide three-dimensional images with a sub-micrometric spatial resolution could also be used to characterize the membranes. X-ray laboratory tomography

could also provide sub-micrometric images but it would require a much higher acquisition time per scan for images corresponding to a lower signal to noise ratio, i.e.,  $\sim 1$  night vs 10 min.

### 2.3. Calculation of Transport and Elasto-Acoustic Properties

In the following subsections, we review the technical background pertaining to pore-scale computations on the generated microstructural samples, including the prediction of both the transport parameters and the elasto-acoustic properties (in Sec. 2.3.1 and Sec. 2.3.2, respectively).

#### 2.3.1. Elementary Transport Processes

In this section, we focus on the determination of macroscopic transport properties, solving local equations supplemented with adequate boundary conditions. More detailed presentations are given by Adler (1992) [10] and by Auriault, Boutin, and Geindreau (2009) [31]. The media considered in this work are considered to be macroscopically homogeneous, and are described as infinite media filled with replicated periodic unit cells. The elementary volume is a cube of size  $L_i \times L_i \times L_i$  containing  $N_p$  pores. The equations to be solved are classically derived from an asymptotic analysis, as described by Bensoussan et al (1978) [48], Sanchez-Palencia (1980) [49], and in the recent studies by Malinouskaya et al (2008) [50] and Boutin and Geindreau (2010) [14].

Note first that any geometric macroscopic property such as the porosity  $\phi$  and the thermal characteristic length  $\Lambda'$  can be directly obtained from the microstructure:

$$\phi = \int_{\Omega_f} dV / \int_{\Omega} dV, \quad \Lambda' = 2 \int_{\Omega_f} dV / \int_{\partial\Omega} dS, \quad (2)$$

where solid border  $\Omega$  is the volume element (VE),  $\Omega_f$  denotes the fluid volume, and  $\partial\Omega$  is its solid border.

The remaining transport parameters are numerically computed using spatial averaging on the solution fields associated with the problems described below.

#### 1. Thermal permeability

Under the excitation of an external, harmonic source, the excess temperature field originates from a spatially uniform, harmonic heating in the air domain, with perfect absorbing conditions on the solid boundaries. The static thermal permeability satisfies the following equation:

$$k'_0 = \phi \langle u \rangle, \quad (3)$$

where the symbol  $\langle \bullet \rangle$  indicates fluid-phase averaging, that is

$$\langle \bullet \rangle = \frac{1}{\Omega_f} \int_{\Omega_f} \bullet dV,$$

and the scaled,  $\Omega$ -periodic temperature field  $u$  is the solution to the Poisson equation

$$\Delta u = -1 \quad \text{in } \Omega_f, \quad (4)$$

supplemented with the thermostat boundary condition

$$u = 0 \quad \text{on } \partial\Omega. \quad (5)$$

Here  $u$  is assumed to be periodic with a period  $L_i$  along the three directions of space. The quantity  $k'_0$  is a positive definite scalar parameter, which only depends on the geometry of the medium. In this work, the diffusion-controlled reaction problem [51] is solved via the finite element method, using Comsol Multiphysics [52].

#### 2. Viscous characteristic length and tortuosity

Note first that the electric conduction terminology is used below, but the following elements remain valid for a potential flow and therefore for a fluid flow of non-viscous particles (high-frequency regime). The electric conduction problem of a conducting fluid subjected to a macroscopic electric field  $\mathbf{e}$  is governed by the following equations:

$$\nabla \cdot \mathbf{E} = 0 \quad \text{in } \Omega_f, \quad (6a)$$

$$\mathbf{E} = -\nabla\varphi + \mathbf{e} \quad \text{in } \Omega_f, \quad (6b)$$

$$\mathbf{E} \cdot \mathbf{n} = 0 \quad \text{on } \partial\Omega, \quad (6c)$$

$$\varphi \text{ is } \Omega \text{ periodic}, \quad (6d)$$

where  $\mathbf{E}$  denotes the solution exhibiting  $-\nabla\varphi$  as a fluctuating part and  $\mathbf{n}$  is the outward-pointing unit normal to the boundary of the pore region. The potential flow field is, again, determined by the finite element method, and the tortuosity  $\alpha_\infty$  and viscous characteristic length  $\Lambda$  (Appendix A) are obtained as

$$\Lambda = \frac{2 \int_{\Omega_f} \mathbf{E}^2 dV}{\int_{\partial\Omega} \mathbf{E}^2 dS}, \quad \alpha_\infty = \frac{\langle \mathbf{E}^2 \rangle}{\langle \mathbf{E} \rangle^2}. \quad (7)$$

More general tensorial expressions of the tortuosity and viscous characteristic length are given by Auriault et al. (1985) [22], Boutin, Geindreau and Auriault (2009) [31] [Eq. (9.15), Chap. 9], and Boulvert et al. (2019) [53] [Appendix A, Eqs. (A8) and (A9)]. Because the electric field  $\mathbf{e}$  provides a preferred direction, the tortuosity  $\alpha_\infty$  and the viscous characteristic length  $\Lambda$  of a medium are generally direction-dependent for a locally inhomogeneous polydisperse foam: their projections over each space direction may differ, as discussed in Zielinski et al. (2020); see Appendix 3 of Ref. [54].

#### 3. Viscous permeability

The low Reynolds flow of an incompressible Newtonian fluid is governed by the usual Stokes equations

$$\begin{aligned} \mu \Delta \mathbf{v} - \nabla p &= -\nabla p^m \\ \text{with } \nabla \cdot \mathbf{v} &= 0 \quad \text{in } \Omega_f, \end{aligned} \quad (8)$$

where  $\mathbf{v}$ ,  $p$ , and  $\mu$  are the velocity, pressure, and viscosity of the fluid, respectively. The term  $\nabla p^m$  is

a macroscopic pressure gradient acting as a forcing term. In general,  $\mathbf{v}$  satisfies the non-slip conditions at the walls,

$$\mathbf{v} = 0 \quad \text{on} \quad \partial\Omega. \quad (9)$$

It can be shown that

$$\mathbf{v} \text{ and } p \text{ are } \Omega\text{-periodic}, \quad (10)$$

with a period  $L_i$  along the three directions of space. In addition, it is assumed that the macroscopic pressure gradient  $\nabla p^m$  is specified in the form

$$\nabla p^m = |\nabla p^m| \mathbf{e}. \quad (11)$$

Since the system Eqs. (8-10) is linear, it can be shown that

$$\phi(\mathbf{v}) = -\frac{\mathbb{K}}{\mu} \cdot \nabla p^m, \quad (12)$$

where  $\mathbb{K}$  is a positive-definite symmetric tensor. This tensor only depends on the geometry of the system and thus can be simplified when the porous medium possesses geometrical symmetries (Kelvin cell). The static permeability  $k_0$  along the direction specified by the unit vector is calculated as:

$$k_0 = (\mathbb{K} \cdot \mathbf{e}) \cdot \mathbf{e} = -\frac{\mu\phi}{|\nabla p^m|} \langle \mathbf{v} \rangle \cdot \mathbf{e}. \quad (13)$$

Here, pore-network simulations are deployed, following the seminal work by Koplik (1981) [26] (see also references therein) and subsequent developments for monodisperse (Langlois et al., 2018) [27] and polydisperse (Langlois et al., 2021) [55] foam structures.

Since the spatial organization of the polydisperse foam structure introduces stochasticity and direction-dependent estimations, an overall effective transport parameter must be introduced. In this work, this parameter is defined as the average of the values of the macroscopic transport parameter obtained along the three directions of space, for five different pore numbers, and three sets of randomly selected open membranes—hence introducing 45 configurations to be analyzed, for each size  $L_i$  of the periodic unit cell.

### 2.3.2. Elasto-Acoustic Macroscopic Behavior

The phenomenological study of the elasto-acoustic properties of porous media was thoroughly presented by Biot [56, 57]. Important semi-phenomenological models with visco-thermal dissipation mechanisms were later developed by Johnson et al. [23] and Lafarge et al. [24]. In these contributions, the assumption of rigid solid skeleton was made *a priori*. Johnson et al. and Lafarge et al. suggested that two general expressions for the frequency-dependence of the visco-inertial and thermal exchanges between the frame and the saturating fluid can be defined with the two sets of parameters  $(\Lambda, k_0, \alpha_\infty, \phi)$  and  $(\Lambda', k'_0, \phi)$ . The model correctly matches the frequency dependence of the

first two leading terms of the exact result for high frequencies, but only one term for low frequencies. Numerical simulations and experiments have shown that the model by Johnson et al. and Lafarge et al. is very robust (JCAL model). It should be noticed that the results provided by Biot and Johnson-Lafarge can be recovered by using the homogenization theory. In this section, we present a brief summary of this theory, with the aim of predicting the sound absorption of polydisperse foams.

For porous materials having a rigid and motionless skeleton, the equivalent dynamic mass density  $\tilde{\rho}_{eq}$  and the equivalent dynamic bulk modulus  $\tilde{K}_{eq}$  of the material are computed as [58]

$$\tilde{\rho}_{eq}(\omega) = \frac{\alpha_\infty \rho_0}{\phi} \left[ 1 + \frac{\sigma \phi}{j \omega \rho_0 \alpha_\infty} \sqrt{1 + j \frac{4\alpha_\infty^2 \mu \rho_0 \omega}{\sigma^2 \Lambda^2 \phi^2}} \right], \quad (14)$$

and

$$\tilde{K}_{eq}(\omega) = \frac{\gamma P_0 / \phi}{\gamma - (\gamma - 1) \left[ 1 - j \frac{\phi \kappa}{k'_0 C_p \rho_0 \omega} \sqrt{1 + j \frac{4k'_0{}^2 C_p \rho_0 \omega}{\kappa \Lambda'^2 \phi^2}} \right]^{-1}}. \quad (15)$$

In these equations,  $\sigma = \mu/k_0$  is the airflow resistivity,  $\rho_0$  is the density of air,  $P_0$  the atmospheric pressure,  $\gamma = C_p/C_v$  the ratio of heat capacities at constant pressure and volume,  $j$  the imaginary unit and  $\omega = 2\pi f$  the angular frequency. The wave number  $\tilde{k}_{eq}(\omega)$  and the characteristic impedance  $\tilde{Z}_{eq}(\omega)$  are then given by:

$$\begin{aligned} \tilde{k}_{eq}(\omega) &= \omega \sqrt{\tilde{\rho}_{eq}(\omega) / \tilde{K}_{eq}(\omega)}, \\ \tilde{Z}_{eq}(\omega) &= \sqrt{\tilde{\rho}_{eq}(\omega) \tilde{K}_{eq}(\omega)}. \end{aligned} \quad (16)$$

For rigidly backed porous material of thickness  $L_s$ , the sound absorption coefficient at normal incidence is given by:

$$\text{SAC}_{\text{NI}} = 1 - \left| \frac{\tilde{Z}_s - Z_0}{\tilde{Z}_s + Z_0} \right|^2, \quad (17)$$

where  $c_0$  is the sound speed in air,  $Z_0 = \rho_0 c_0$  is the the impedance of the air and  $\tilde{Z}_s$  is the normal incidence surface impedance:

$$\tilde{Z}_s = -j \tilde{Z}_{eq} \cot(\tilde{k}_{eq} L_s). \quad (18)$$

The elasto-acoustic coupling effects due to the deformation and/or vibration of solid phase (solid skeleton and solid walls or membranes) on the absorption coefficient may be taken into account using the Biot-JCAL model [59, 60]. By assuming that the dissipation in the fluid phase is independent of the dissipation occurring in the material

skeleton (the deformation of the pore skeleton does not significantly affect the fluid properties), Biot [56, 57] has considered the existence of two compressional waves and one shear wave in a fluid-saturated porous medium. In a normal acoustic field, the shear wave is not excited and only the compression waves can propagate. The surface impedance at normal incidence in that case is predicted by [58]:

$$\tilde{Z}_s = -j \frac{(\tilde{Z}_1^s \tilde{Z}_2^f \mu_2 - \tilde{Z}_2^s \tilde{Z}_1^f \mu_1)}{D}, \quad (19)$$

Here,  $\tilde{Z}_i^s$  and  $\tilde{Z}_i^f$  (with  $i = 1, 2$ ) are the characteristic impedances in the solid (superscript  $s$ ) and fluid phase (superscript  $f$ ) for the first (index 1) and second (index 2) Biot compressional waves. The expressions of  $\tilde{Z}_i^s$ ,  $\tilde{Z}_i^f$ ,  $D$ ,  $\mu_1$ , and  $\mu_2$  are provided in Appendix B.

Finally, the sound absorption coefficient at normal incidence including elastic effects can also be calculated by using Eq. 17 and by relying on Eq. 19 and subsequent equations to compute the corresponding surface impedance.

### 3. Comparison Between Multi-Scale Computations and Experimental Measurements

#### 3.1. Direct Characterization of Macroscopic Properties

In order to evaluate our methodology, experimental data measured at macro-scale were used. The porosity  $\phi$  and the permeability  $k_0$  were measured on six cylindrical samples of diameter 40 [mm] and length 21 [mm]. The global porosity was measured by comparison of four different masses at four static pressures from which the open porosity and the true mass density  $\rho_1$  are deduced using the ideal gas law [61]. Permeability was measured with air in the six samples from the determination of the static and flow resistivity  $\sigma = \mu/k_0$ , in a laminar regime, following the specification of ISO 9053-1:2018. The corresponding experimental data are reported in Tab. 2.

Finally, an experimental determination of the viscoelastic parameters, namely the Young's modulus  $E$ , the Poisson ratio  $\nu$  and the loss factor  $\eta$  are obtained through a quasi-static mechanical characterization method as originally proposed by Mariez *et al.* [62] and extended by Langlois *et al.* [63].

The Young's modulus data are also displayed in Fig. 6 for different compression rates, and they are seen to lower as the compression rates are reduced. The measured Young's modulus differs by a factor of 3 in the studied range of compression rates which varied from 0.5 to 3 percent. It is important to note that the extrapolated value at a compression rate equal to zero is very sensitive to the experimental data in the range [0.5% – 1.5%]. Chevillote *et al.* (2020) [64] also observed that this sensitivity of the Young's modulus to the compression rate may result in scattered experimental data. Here, a power law for the extrapolation is chosen, yielding  $E \approx 140$  [kPa] at zero compression rate.

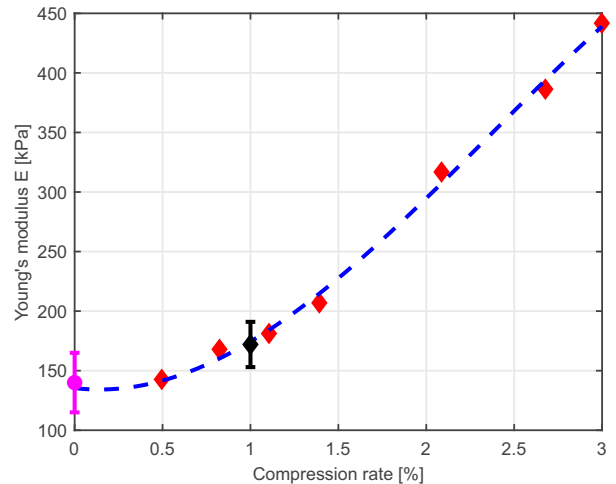


Figure 6: (Color online) Young's modulus as a function of the compression rate. The mean and corresponding standard deviation measured at 1% of compression rate are in black. The mean and corresponding standard deviation extrapolated at 0% of compression rate are provided in magenta.

Of course, the value of the Young's modulus results generally from the mounting condition of the sample which are prescribed for a specific application. The influence of the Young's modulus variation on the sound absorption coefficient will be specifically discussed in Sec. 3.3.

#### 3.2. Prediction of Macroscopic Transport Parameters

The evolution of the mean and standard deviation for dimensionless transport properties as a function of the number of pores  $N_p$  is shown in Fig. 7. It is observed that average values for the computed geometrical and transport parameters remain fairly constant for  $N_p \geq 50$ , while a reduction in the order of 10% of the average value for the dispersion parameter requires a significant increase of the number of reconstructed pores. Notice that  $N_p = 453$  corresponds to  $L/\langle d \rangle \approx 10$ .

Computed and measured macroscopic parameters can be found in Tab. 3, where computational results are obtained for  $N_p = 453$ . The relatively large dispersion of the results mainly observed for  $k_0$  and  $\alpha_\infty$  is attributed to the pore size and shape local inhomogeneity, rather than a possible anisotropy; see Tab. 4. Recall that the average is taken over all principal directions and over several statistically identical geometric configurations (see the averaging procedure described in Sec. 2.3.1), the predicted values of viscous permeability  $k_0$  are shown to be in close agreement with measurements. It is noteworthy that the unusually high value of the thermal over viscous characteristic lengths ratio  $\Lambda'/\Lambda = 4.56$  is another interesting effect of membranes at macro-scale. We also see a drastic effect of both: (i) disorder (Fig. 3) expressed through a strongly inhomogeneous pore structure and (ii) a significant proportion of fully closed membranes together with a small

$\rho_1$ [ $kg/m^3$ ]	$\phi$ [-]	$\sigma$ [ $Ns/m^4$ ]	$E$ [ $kPa$ ]	$\nu$ [-]	$\eta$ [-]
$13.37 \pm 0.19$	$0.92 \pm 0.01$	$67500 \pm 9900$	$140 \pm 25$	$0.46 \pm 0.02$	$0.157 \pm 0.005$

Table 2: Experimental data of the polydisperse foam measured at macro-scale.

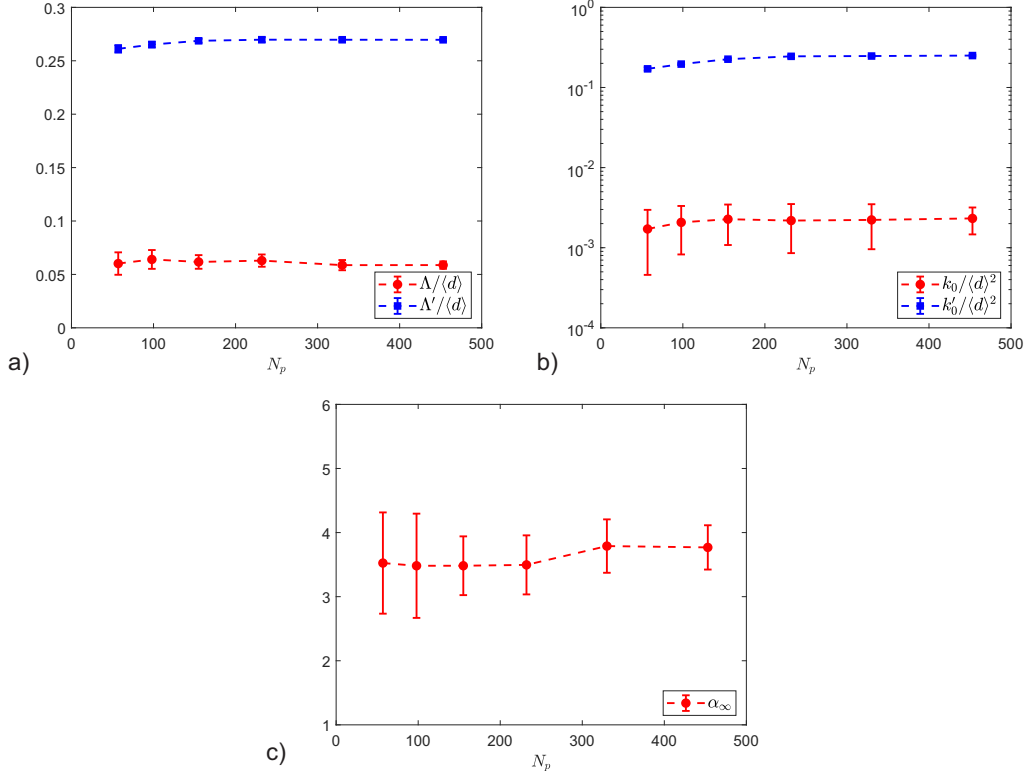


Figure 7: (Color online) Dimensionless transport properties versus pore number  $N_p$ , the error bars represents the standard deviations.

opening of the remaining apertures (Tab. 1) on tortuosity, which yields  $\alpha_\infty = 3.77 \pm 0.35$ .

We next studied the influence of membrane descriptors introduced above (Sec. 2.1.2) and the variation of them around the experimentally determined values on the predicted transport parameters. The membrane descriptors used are the proportion of non fully-closed membranes  $x_o$  and the aperture ratio of the open membranes  $t_o$ . The sensitivity of predictions to variations in either  $t_o$  (blue) or  $x_o$  (red) is illustrated in Fig. 8. Note that the mean values of the transport parameters for each microstructural configuration ( $x_o$ ,  $t_o$ ) are calculated from 45 values (corresponding to 5 structures, 3 sets of randomly selected membranes, and 3 principal directions). In this figure, results are displayed in a dimensionless form by using the average pore size  $\langle d \rangle$  as a reference dimension of the pore size. The range of experimental dispersion of these parameters  $x_o$  and  $t_o$  is also reported on Fig. 8 and provides a graphical analysis of the numerical sensitivity with respect to perturbation in the characterized inputs. It is clear that  $x_o$  or  $t_o$  reduces membrane content, which leads to an increase of the porous structure viscous permeability  $k_0$  and a reduction of the tortuosity  $\alpha_\infty$ , as expected. It

is also worth to point out that the pore-volume-to-surface ratio increases by decreasing the membrane content, and so do  $\Lambda'$  and  $\Lambda$ , which are strongly correlated. We also notice that the static thermal permeability  $k'_0$  is relatively independent to the membrane content when compared to the static viscous one  $k_0$ , since  $k'_0$  is not directly related to the connectivity of pore space [65]. Contrary to the results of the static viscous permeability, the results of the static thermal permeability are independent of a specified direction (scalar quantity). It is remarkable that the independent variation of  $x_o$  or  $t_o$  gives similar qualitative trends, although an accurate quantitative prediction of all the transport parameters requires a detailed knowledge of each membrane descriptor.

From Fig. 8c, it can be seen that, around the characterized mean values of the membrane content  $\langle x_o \rangle = 0.28$ ,  $\langle t_o \rangle = 0.51$ , the effect of closing supplementary membranes is larger than the effect of reducing the aperture ratio of open membranes on tortuosity (larger slope). We get as a consequence that the ratio of open membranes  $x_o$  should be characterized with great care, and that a significant increase of the tortuosity  $\alpha_\infty$  could be obtained by lowering the amount of available open pores (at the expense

	$\phi(-)$	$k_0 (10^{-10}m^2)$	$\alpha_\infty(-)$	$\Lambda(\mu m)$	$\Lambda'(\mu m)$	$k'_0 (10^{-10}m^2)$
Measurements	$0.92 \pm 0.01$	$2.73 \pm 0.34$				
Computations		$2.83 \pm 0.57$	$3.77 \pm 0.35$	$59 \pm 3$	$270 \pm 1$	$324 \pm 8$

Table 3: Macroscopic transport parameters: measurements and computational results

	$k_0 (10^{-10}m^2)$			$k'_0 (10^{-10}m^2)$	$\Lambda(\mu m)$			$\Lambda'(\mu m)$	$\alpha_\infty(-)$		
	$x$	$y$	$z$		$x$	$y$	$z$		$x$	$y$	$z$
Structure 1	3.09	2.86	2.67	331	60.6	60.6	55.6	269.1	3.58	3.65	3.93
Structure 2	2.92	2.78	2.67	327	59.2	57.0	61.8	269.5	3.65	3.98	3.62
Structure 3	2.66	2.80	3.16	330	58.5	62.7	60.0	271.2	3.88	3.40	3.69
Structure 4	2.71	2.62	2.81	314	57.7	55.7	57.4	269.5	3.72	3.91	3.98
Structure 5	3.02	2.83	3.57	320	60.5	58.3	55.5	268.8	3.52	3.80	4.22

Table 4: Macroscopic transport parameters: computational results for different structures. Here, the term "structure" refers to a foam sample containing 453 pores and reconstructed using the methodology described in Sec. 2.2.1. Recall that each transport parameter reported in the table corresponds to an average over three sets of randomly selected open membranes (as described at the end of Sec. 2.3.1).

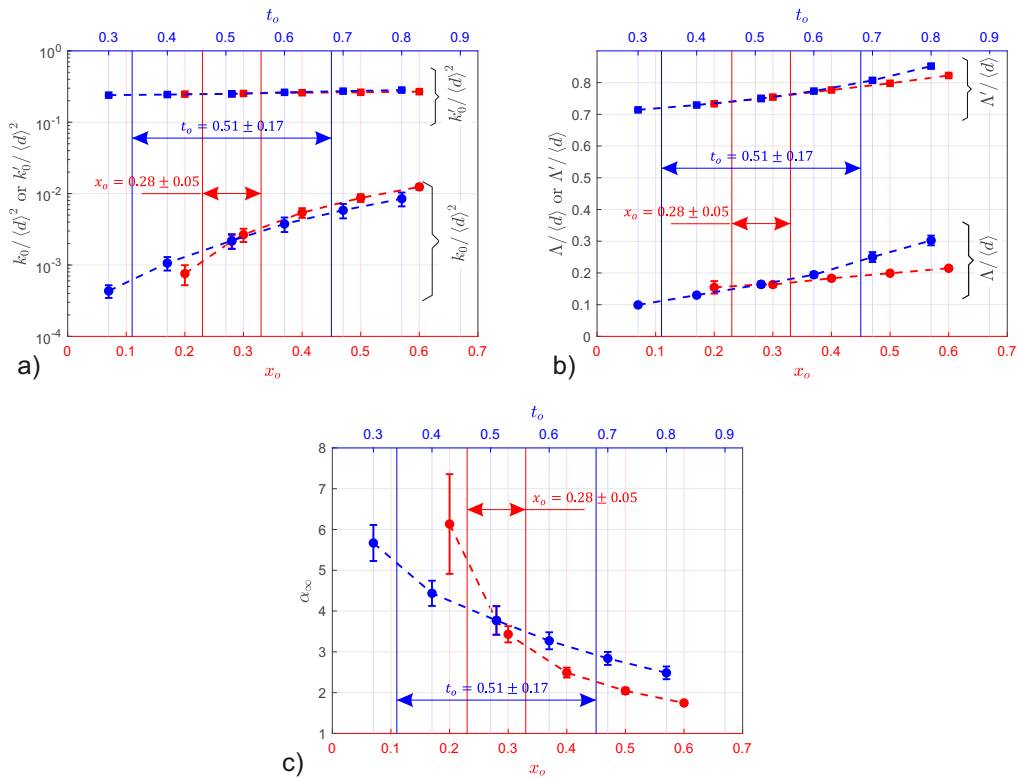


Figure 8: (Color online) The membrane content ( $x_o$  and  $t_o$ ) dependence of the transport parameters. The red symbols correspond to the case of  $t_o = 0.51$ , the blue symbols correspond to the case of  $x_o = 0.28$ . The intersection points correspond to the mean measured values ( $x_o = 0.28$  and  $t_o = 0.51$ ). The error bars correspond to standard deviations.

of largest standard deviations of  $\alpha_\infty$  induced by greater anisotropy). On the other hand, increasing the opening ratio  $t_o$  has a larger effect on the viscous characteristic length  $\Lambda$  increase than increasing the proportion of open membranes  $x_o$  (Fig. 8b), since the weighting procedure implied by Eq. 7 substantially favors smaller apertures.

### 3.3. Determination of the Sound Absorption Coefficient

The sound absorption coefficient at normal incidence  $SAC_{NI}$  of the polydisperse foam sample backed with a rigid wall was studied using a three-microphone impedance tube setup [66, 67]. The same series of six cylindrical foam samples with a thickness of 21mm were used to characterize the porosity  $\phi$ , the resistivity  $\sigma$  (Sec. 3.1) and the sound absorption coefficient at normal incidence  $SAC_{NI}$ . A thin

layer of Teflon was used around the cylindrical samples to avoid air leakage between the tube wall and the foam samples; this implies that a slight compression of the samples was applied in the radial direction during impedance tube measurements.

The prediction of the  $SAC_{NI}$  derived from the Johnson-Champoux-Allard-Lafarge model (JCAL) assuming rigid skeleton (Eqs. 14-18) using computed transport parameters as input data to the model (Tab. 3) is compared to experimental data including a dispersion envelope, Fig. 9. A satisfactory agreement requires the knowledge of viscoelastic parameters  $(E, \nu, \eta)$  from Tab. 2 as additional inputs through a Biot-JCAL model (Eq. 18 replaced by Eq. 19), suggesting a strong elasto-acoustic coupling in which the quality of the agreement depends strongly upon the value of the Young's modulus  $E$ . The elastic effects dramatically shift the second sound absorption peak towards lower frequencies, which originates from the modification of the intrinsic damped complex wavelength. A frame acoustical excitability criterion (FAE), which states that when the FAE is superior to a critical value of 2 [ $MW/Kg$ ] ( $FAE = \sigma E t^2 / \rho_1^2 R^2$ ,  $t$  and  $R$  are the thickness and radius of a disk-shaped porous sample), the influence of the circumferential edge constraint on the elasto-acoustic behavior of the foam sample becomes important and the solid phase vibrates, is well verified (here,  $FAE \approx 57 [MW/Kg]$ ); cf. Pilon *et al.*, 2003 [68].

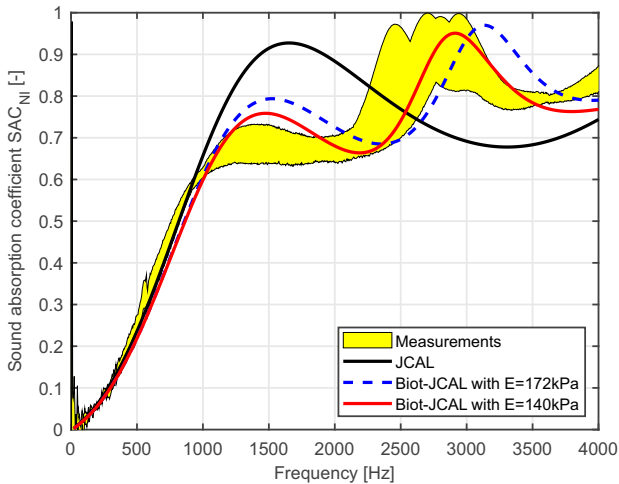


Figure 9: (Color online) Sound acoustical coefficient. Sample thickness: 21 [ $mm$ ].

We note that measurements with impedance tube may lead to a small pre-compression of the foam sample, which is consistent with a compression rate around 0.5% corresponding to the characterized Young's modulus (Fig. 6 and 9). The complexity of the predictive models could be further increased by using for example, a high order axisymmetric finite elements [69] based on the mixed ( $u-p$ ) Biot poroelastic formulation [70], with a bonded condition applied on the circumference of the sample to better de-

scribe the circumferential edge constraint effect. Although we could expect to see further improvements in the quality of the agreement, the axisymmetric finite elements Biot poroelastic formulation would require adjusting the value of the Young's modulus to account for the circumferential edge constraint, while our aim is still to avoid model fitting. Finally, a complete quantitative experimental characterization of the transport parameters of a porous material in a three-microphone impedance tube via two transfer functions is in principle possible [66, 67] (see, e.g., the statistical inversion methods described in [71]). However, the latter analytic inversion method requires a rigid frame assumption (as assumed in the JCAL model). The elasto-acoustic behavior illustrated through Fig. 9 (Biot-JCAL with  $E = 140 [kPa]$ ), clearly shows why the indirect inversion method [66, 67] typically fails for such poroelastic structures.

In order to evaluate the contribution of viscous and thermal dissipation on the SAC curve, based on the (elasto-visco-thermal) Biot-JCAL model with characterized Young's modulus ( $E = 140 [kPa]$ ), it is possible to define the Biot-J model which does not take into account the thermal effects by modifying the effective bulk modulus in Eq. 15:

$$K_{eq}(\omega) = \frac{\gamma P_0}{\phi}. \quad (20)$$

In the same way, an elasto-thermal model (Biot-CAL) is defined by discarding the viscous effects while keeping the effective bulk modulus in Eq. 15 but modifying the effective density in Eq. 14:

$$\rho_{eq}(\omega) = \frac{\alpha_{\infty} \rho_0}{\phi}. \quad (21)$$

Fig. 10 compares the computed sound absorption coefficient curves with Biot-JCAL, Biot-J and Biot-CAL together with the measured one. It can be shown that the Biot-CAL which does not take into account the viscous effect is not convincing. In addition, small deviations between Biot-JCAL and Biot-J show the importance of viscous and elastic effect. We therefore conclude that for foams having a large amount of membranes, the absorption is mainly controlled by the viscous flow and the elastic skeleton effects; whereas the thermal losses do not play a significant role on the sound absorption for this kind of foams.

We next explore the influence of the membrane descriptors  $x_o$  and  $t_o$  on the sound absorption coefficient at normal incidence for all samples and a (poroelastic) layer thickness of 21 [ $mm$ ]; see Fig. 11. Here, similarly to the analysis illustrated in Fig. 8, one parameter (that is,  $x_o$  or  $t_o$ ) is allowed to vary, while the other is set to its mean value. These results show that a small increase of the fraction of open membranes,  $x_o$ , could be slightly beneficial in the frequency range [ $1200Hz - 2500Hz$ ] ( $x_o = 0.3$ ), without observing a reduced sound absorption in the remaining frequency range. The parametric modification of the fraction of open membranes  $x_o$  at constant aperture

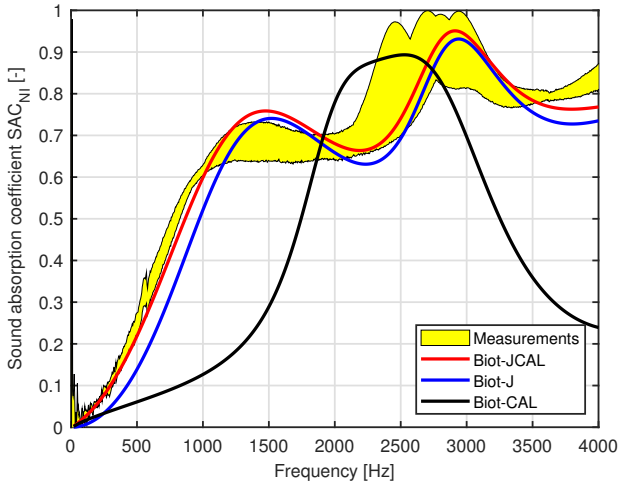


Figure 10: (Color online) Characterized and computed sound acoustical coefficient ( $E = 140$  [kPa]). Sample thickness: 21 [mm].

ratio of open membranes  $t_o$  indicates that a reduction of  $x_o$  increases the  $SAC_{NI}$  before 700 [Hz], but there is a drop of the  $SAC_{NI}$  particularly in the frequency range [700Hz – 2000Hz] ( $x_o = 0.2$ ). An increase of  $x_o$  basically increases the value of the first sound absorption peak, but also shift its frequency towards higher frequencies ( $x_o = 0.4 - 0.6$ ).

Again, to gain some understanding on the sensitivity of the model to the aperture ratio of open membranes  $t_o$ , we performed for the case of the fraction of open membranes  $x_o = 0.28$  a series of simulations with respect to perturbation of  $t_o$ . Modifying in the model the aperture ratio with a step of 0.1 induces some strong modifications of the sound absorption between 1000Hz and 2500Hz (Fig. 11a). Increasing  $t_o$  also results in an increase of the maximum value of the first sound absorption peak and shift this peak towards higher frequencies.

#### 4. Conclusion

We have developed a multi-scale approach to establish a link between the microstructure of a polydisperse foam and its fluid-flow properties. The analyzed experimental microstructure includes more than two thousand pores with a wide distribution of pore sizes and shapes, and the membranes separating two pores are either closed or open with a specific aperture ratio. To characterize the pore space geometry, we used computed microtomography with a spatial resolution of a few micrometers per voxel and image processing techniques. Lognormal distributions of pore size and sphericity were used to reconstruct geometrical models having statistically representative properties, including morphological indicators, as well as the proportion of fully closed membranes  $x_c$  and the average of aperture ratio  $t_o$  for the randomly-distributed open membranes. We found that the transport properties become

relatively independent of the size of the model when the number of pores in the reconstructed domain contains at least ten average pore diameter per representative volume element side. This suggests that sufficiently large polydisperse foam structures are needed to fully capture the local heterogeneity content of the foam morphology. Deploying finite element and pore-network simulations, we then obtained transport parameters and fed them as inputs in order to predict sound absorption at normal incidence. In this setting, visco-elastic parameters were not numerically determined and were directly measured at macro-scale. We found that combining visco-elastic and transport parameters through a Biot-JCAL model provides a good prediction of the measured sound absorption at normal incidence. This shows that the greater morphological information content contained in a highly polydisperse foam sample with a membrane content could be used for designing elasto-acoustic properties of locally inhomogeneous poro-elastic materials. Moreover, our work demonstrates that advanced stochastic geometry combined with computational methods can be very useful in establishing structure-property relationships of polydisperse foams.

#### Acknowledgments

This work was supported by the Association Nationale de la Recherche et de la Technologie (ANRT) and Trèves Group under CIFRE agreement No. 2017/1908. The support of the Fédération Francilienne de Mécanique (F2M) is also gratefully acknowledged. This work has also benefited from a French government grant managed by ANR within the frame of the national program Investments for the Future ANR-11-LABX-022-01.

#### Appendix A. Numerical Method for Viscous Length

We consider the singular response of a specific class of wedge-shaped geometries in the high-frequency limit defined in Sec. 2.3.1. Specifically, we seek a numerical estimation of  $\Lambda$  for polydisperse solid foams in which the solid wall thickness (membrane) is much smaller than the average pore size (that is, the apex angle of the wedge tends to zero); see Fig. A.12.

We present a numerical solution to the closure problem (Eqs. 6a-6d) for a 3D Kelvin-cell structure of size  $D_p$  when generated with a pore wall thickness equal to zero and a pore opening of radius  $r_o$ ; this configuration is referred to as  $K0$  below (see Fig. A.13; the mesh corresponding to the pore domain and a magnified view of the aperture region are shown in panel b)). As presented in Sec. 2.3.1, the viscous characteristic length  $\Lambda$  can be computed as

$$\Lambda = \frac{2I_V}{I_S}, \quad (\text{A.1})$$

where  $I_V = \int_{\Omega_f} \mathbf{E}^2 dV$  and  $I_S = \int_{\partial\Omega} \mathbf{E}^2 dS$  denote volume and surface integrals of the electric field  $\mathbf{E}$ , respectively.

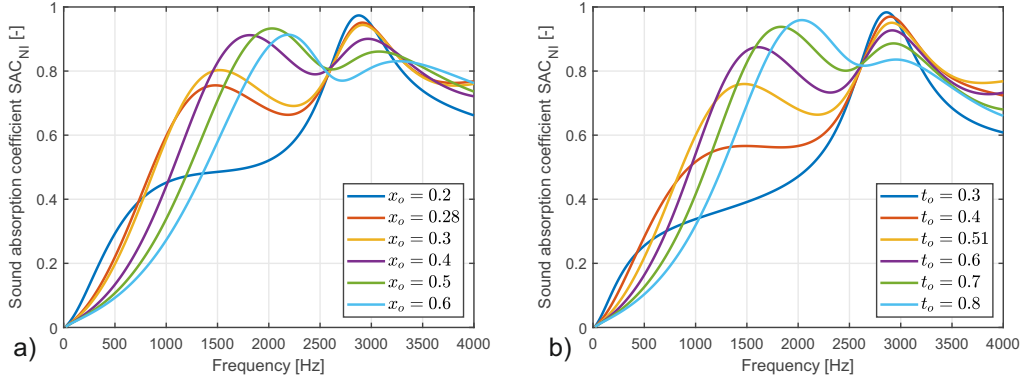


Figure 11: (Color online) Sound absorption coefficients of the foams: (a) with different opened membrane fraction (at constant aperture ratio,  $t_o = 0.51$ ); (b) with different membrane aperture ratios (at constant open membrane fraction,  $x_o = 0.28$ ). Sample thickness: 21 [mm].

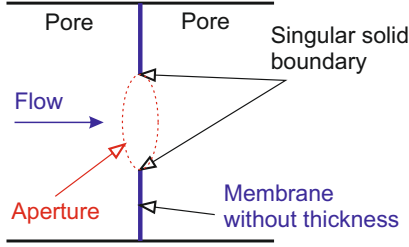


Figure A.12: (Color online) Illustration of the singularity of the solid boundary in a structure without membrane thickness.

The above representation in terms of volume and surface integrals allows for the prediction of  $\Lambda$  on very thin membranes with smooth-shaped geometries to be conveniently studied from a computational standpoint. Because the electric field  $\mathbf{E}$  is a function of the gradient of the scaled electric potential  $\varphi$  and since the latter may not be smooth in the vicinity of the singularity of  $\partial\Omega$  if  $\Omega_f$  has a sharp edge,  $\mathbf{E}$  may be very singular [72]. This implies that a specific numerical treatment must be followed in the computation of  $\mathbf{E}^2$  and its integral. This behavior is quantitatively illustrated in Fig. A.14, where the parameters  $\alpha_\infty$ ,  $I_V$ ,  $I_S$ , and  $\Lambda$  are computed for different characteristic element sizes. It is seen that the predictions of  $\alpha_\infty$  and  $I_V$  are relatively insensitive to mesh refinement, while substantial variations of  $I_S$  and  $\Lambda$  are observed as  $h_e/D_p \rightarrow 0$ . To address this problem and obtain a robust estimation of  $\Lambda$ , we seek a relation between a solid foam structure where the membrane has a given thickness  $e_m$ , and an equivalent solid foam structure where the membrane thickness is set to zero but mesh size  $h_e$  is close to  $e_m$ . Two different geometrical configurations are proposed. In model 1, the membrane thickness is set to  $e_m$  and a fillet of radius  $e_m/2$  is introduced to avoid the sharp edge effect (see Fig. A.15). To ensure that the solution is accurately calculated, a mesh size smaller than  $e_m/10$  is used. In model 2, the membrane thickness is set to zero and the element size is chosen as  $e_m$  in the vicinity of the aperture (see

Fig. A.13b).

In Fig. A.16, the surface integral  $I_S$ , normalized by  $D_p^2$ , is plotted as a function of (i) the membrane thickness  $e_m$ , normalized by  $D_p$  [model 1] or (ii) the mesh size  $h_e$  normalized by  $D_p$  [model 2]. Three different Kelvin-structures are generated using different solid membrane contents: for  $K0$ , all solid membranes are opened; for  $K1$ , only solid membranes with square faces are opened; for  $K2$ , only solid membranes with hexagonal faces are opened. From Fig. A.16, it is seen that the normalized surface integral  $I_S/D_p^2$  behaves as a logarithmic form  $A \log_{10}(x/D_p) + B$ , with adjusted coefficients  $A$  and  $B$ ; and that the numerical results provided by model 1 and model 2 agree very well, particularly when  $x/D_p \leq 10^{-3}$  ( $x$  is  $e_m$  or  $h_e$ ;  $A$  and  $B$  depend on the geometry). It is worth mentioning that these conclusions remain valid for various ratios of  $r_o/D_p$  (these results are not reported below, for the sake of conciseness).

In conclusion, the viscous characteristic length  $\Lambda$  can be accurately calculated by setting the membrane thickness  $e_m$  to zero and by imposing a mesh size  $h_e = e_m$  in the vicinity of the aperture. The logarithmic behavior of the normalized surface integral,  $I_S/D_p^2 = A \log_{10}(h_e/D_p) + B$ , also provides a way to determine  $\Lambda$  for thin membranes by determining the constants  $A$  and  $B$  with two raw mesh sizes.

## Appendix B. Surface impedance in a normal acoustic field for a layer of elastic porous material

For porous materials having an elastic frame, the Biot theory is used to predict their behavior in a normal acoustic field [58]. The surface impedance at normal incidence backed by an impervious rigid wall of a layer of elastic porous material was provided by Eq. 19 in Section 2.3. In this equation, the characteristic impedances in the solid (superscript  $s$ ) and fluid phase (superscript  $f$ ) for the first (index 1) and second (index 2) Biot compressional waves,

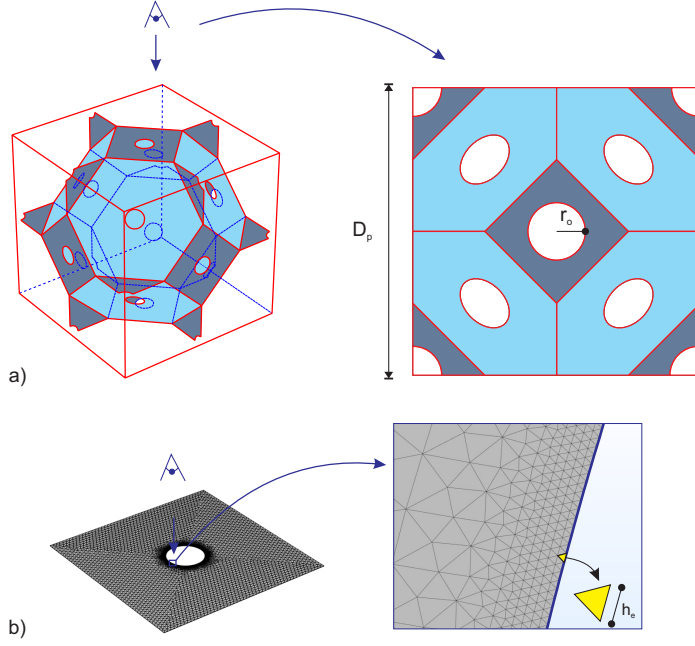


Figure A.13: (Color online) a) Configuration K0 of Kelvin-cell structure. b) Finite element mesh around the aperture.

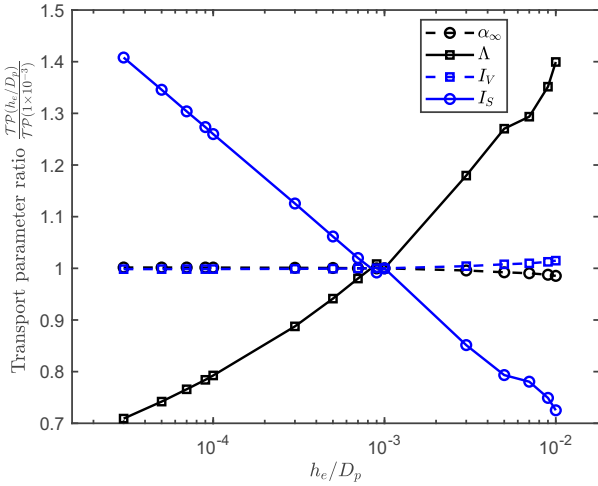


Figure A.14: (Color online) Evolution of various normalized transport parameters ( $\mathcal{TP}$ ) as a function of the ratio  $h_e/D_p$ . Here,  $r_o/D_p = 0.1$ ,  $D_p = 1$  [mm].

$\tilde{Z}_i^s$  and  $\tilde{Z}_i^f$  can be written as:

$$\tilde{Z}_i^s = (P + Q\mu_i) \frac{\delta_i}{\omega}, \quad \tilde{Z}_i^f = \left(R + \frac{Q}{\mu_i}\right) \frac{\delta_i}{\phi\omega}. \quad (\text{B.1})$$

In addition,  $\delta_1$  and  $\delta_2$  are the complex wave numbers of the two compressional waves, defined as

$$\delta_i^2 = \frac{\omega^2}{2(PR - Q^2)} \left[ P\tilde{\rho}_{22} + R\tilde{\rho}_{11} - 2Q\tilde{\rho}_{12} \mp \sqrt{\Delta} \right], \quad (\text{B.2})$$

$i = 1(-), 2(+)$ ,

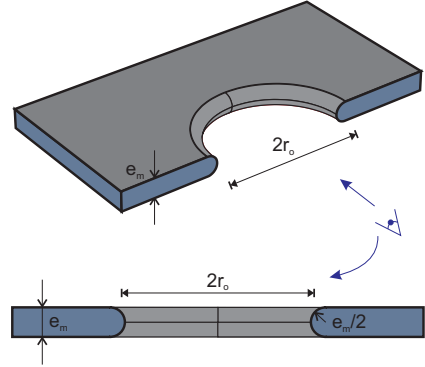


Figure A.15: (Color online) Sketch of a solid membrane of thickness  $e_m$  with a fillet of radius  $e_m/2$ .

with

$$\Delta = [P\tilde{\rho}_{22} + R\tilde{\rho}_{11} - 2Q\tilde{\rho}_{12}]^2 - 4(PR - Q^2)(\tilde{\rho}_{11}\tilde{\rho}_{22} - \tilde{\rho}_{12}^2). \quad (\text{B.3})$$

The parameters  $D$ ,  $\mu_1$  and  $\mu_2$  are given by:

$$D = (1 - \phi + \phi\mu_2) \left[ \tilde{Z}_1^s - (1 - \phi) \tilde{Z}_1^f \mu_1 \right] \tan(\delta_2 L_s) + (1 - \phi + \phi\mu_1) \left[ (1 - \phi) \tilde{Z}_2^f \mu_2 - \tilde{Z}_2^s \right] \tan(\delta_1 L_s), \quad (\text{B.4})$$

$$\mu_i = \frac{P\delta_i^2 - \omega^2 \tilde{\rho}_{11}}{\omega^2 \tilde{\rho}_{12} - Q\delta_i^2}, \quad i = 1, 2.$$

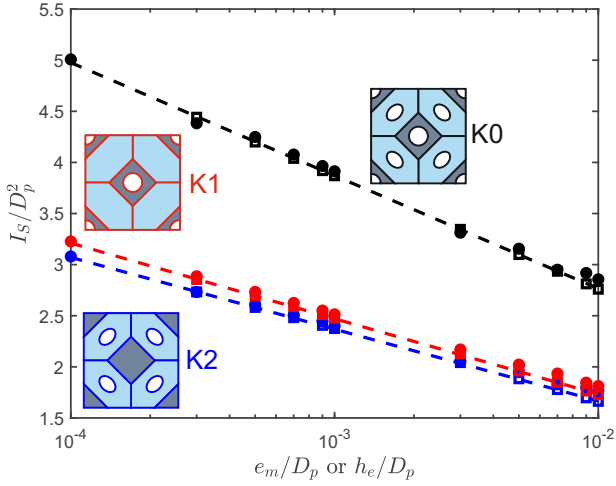


Figure A.16: (Color online) Normalized surface integral  $I_S/D_p^2$  as a function of  $e_m/D_p$  (non-zero thickness, square marker) or  $h_e/D_p$  (thickness set to zero, circular marker) for different Kelvin-cell configurations.  $r_o/D_p = 0.1$ ,  $D_p = 1\text{mm}$ . The dashed lines correspond to adjusted curves of the form  $A \log_{10}(x/D_p) + B$ , with  $x$  is  $e_m$  or  $h_e$ .

Additional parameters  $P$ ,  $Q$ , and  $R$  denote the following elasticity coefficients:

$$\begin{aligned} P &= \frac{4}{3}N + K_b + \frac{(1-\phi)^2}{\phi}K_f, \\ Q &= K_f(1-\phi), \\ R &= \phi K_f, \end{aligned} \quad (\text{B.5})$$

where  $K_f = \phi K_{eq}$  is the bulk modulus of the effective fluid and the modulus of solid frame  $K_b$  is evaluated as

$$K_b = \frac{2N_b(\nu+1)}{3(1-2\nu)}. \quad (\text{B.6})$$

The shear modulus of the frame  $N_b$  is obtained from the visco-elastic parameters of the porous material ( $E, \nu, \eta$ ) as

$$N_b = \frac{E(1+j\eta)}{2(1+\nu)}. \quad (\text{B.7})$$

Biot's modified mass densities are expressed as [59, 60]:

$$\begin{aligned} \tilde{\rho}_{22} &= \phi^2 \tilde{\rho}_{eq}, \\ \tilde{\rho}_{12} &= \phi \rho_0 - \tilde{\rho}_{22}, \\ \tilde{\rho}_{11} &= \rho_1 - \tilde{\rho}_{12}. \end{aligned} \quad (\text{B.8})$$

## References

- [1] A. M. Kraynik, D. A. Reinelt, F. van Swol, Structure of random foam, *Physical Review Letters* 93 (20) (2004) 208301. doi:10.1103/physrevlett.93.208301.
- [2] A. M. Kraynik, D. A. Reinelt, F. van Swol, Structure of random bidisperse foam, *Colloids and Surfaces A: Physicochemical and Engineering Aspects* 263 (1-3) (2005) 11–17. doi:10.1016/j.colsurfa.2005.02.037.
- [3] M. D. Montminy, A. R. Tannenbaum, C. W. Macosko, The 3D structure of real polymer foams, *Journal of Colloid and Interface Science* 280 (2004) 202–211. doi:10.1016/j.jcis.2004.07.032.
- [4] O. Gerbault, F. Buyens, V. Mourzenko, A. Momponteil, A. Vabre, J.-F. Thovert, P. Adler, Transport properties of real metallic foams, *Journal of colloid and interface science* 342 (1) (2010) 155–165. doi:10.1016/j.jcis.2009.10.011.
- [5] J. Skibinski, K. Cwieka, T. Kowalkowski, B. Wysocki, T. Wejrzanowski, K. J. Kurzydowski, The influence of pore size variation on the pressure drop in open-cell foams, *Materials & Design* 87 (2015) 650–655. doi:10.1016/j.matdes.2015.08.079.
- [6] D. Westhoff, J. Skibinski, O. Sedivý, B. Wysocki, T. Wejrzanowski, V. Schmidt, Investigation of the relationship between morphology and permeability for open-cell foams using virtual materials testing, *Materials & Design* 147 (2018) 1–10. doi:10.1016/j.matdes.2018.03.022.
- [7] M. Neumann, O. Stenzel, F. Willot, L. Holzer, V. Schmidt, Quantifying the influence of microstructure on effective conductivity and permeability: virtual materials testing, *International Journal of Solids and Structures* 184 (2020) 211–220. doi:10.1016/j.ijsolstr.2019.03.028.
- [8] R. Quey, L. Renversade, Optimal polyhedral description of 3D polycrystals: method and application to statistical and synchrotron x-ray diffraction data, *Computer Methods in Applied Mechanics and Engineering* 330 (2018) 308–333. doi:10.1016/j.cma.2017.10.029.
- [9] S. Torquato, *Random Heterogeneous Materials: Microstructure and Macroscopic Properties*, 1st Edition, Interdisciplinary Applied Mathematics N16, Springer-Verlag New York, 2002.
- [10] P. M. Adler, *Porous media: geometry and transports*, Butterworth-Heinemann series in chemical engineering, Butterworth-Heinemann, 1992.
- [11] K. Gao, J. van Dommelen, M. Geers, Microstructure characterization and homogenization of acoustic polyurethane foams: Measurements and simulations, *International Journal of Solids and Structures* 100 (2016) 536–546. doi:10.1016/j.ijsolstr.2016.09.024.
- [12] V. H. Trinh, V. Langlois, J. Guillemot, C. Perrot, Y. Khidas, O. Pitois, Tuning membrane content of sound absorbing cellular foams: Fabrication, experimental evidence and multiscale numerical simulations, *Materials & Design* 162 (2019) 345–361. doi:10.1016/j.matdes.2018.11.023.
- [13] C. Boutin, Study of permeability by periodic and self-consistent homogenisation, *European Journal of Mechanics-A/Solids* 19 (4) (2000) 603–632. doi:10.1016/s0997-7538(00)00174-1.
- [14] C. Boutin, C. Geindreau, Periodic homogenization and consistent estimates of transport parameters through sphere and polyhedron packings in the whole porosity range, *Physical review E* 82 (3) (2010) 036313. doi:10.1103/physreve.82.036313.
- [15] R. Verdejo, R. Stämpfli, M. Alvarez-Lainez, S. Mourad, M. Rodriguez-Perez, P. Brühwiler, M. Shaffer, Enhanced acoustic damping in flexible polyurethane foams filled with carbon nanotubes, *Composites Science and Technology* 69 (10) (2009) 1564–1569. doi:10.1016/j.compscitech.2008.07.003.
- [16] I. Vecchio, C. Redenbach, K. Schladitz, A. M. Kraynik, Improved models of solid foams based on soap froth, *Computational Materials Science* 120 (2016) 60–69. doi:10.1016/j.commatsci.2016.03.029.
- [17] O. Doutres, N. Atalla, K. Dong, A semi-phenomenological model to predict the acoustic behavior of fully and partially reticulated polyurethane foams, *Journal of Applied Physics* 113 (5) (2013) 054901. doi:10.1063/1.4789595.
- [18] C. P. Gonatas, J. S. Leigh, A. G. Yodh, J. A. Glazier, B. Prause, Magnetic resonance images of coarsening inside a foam, *Phys. Rev. Lett.* 75 (1995) 573–576. doi:10.1103/PhysRevLett.75.573. URL <https://link.aps.org/doi/10.1103/PhysRevLett.75.573>
- [19] C. Monnereau, M. Vignes-Adler, Dynamics of 3d real foam coarsening, *Phys. Rev. Lett.* 80 (1998) 5228–5231.

- doi:10.1103/PhysRevLett.80.5228.  
URL <https://link.aps.org/doi/10.1103/PhysRevLett.80.5228>
- [20] S. Hilgenfeldt, A. M. Kraynik, S. A. Koehler, H. A. Stone, An accurate von neumann's law for three-dimensional foams, *Phys. Rev. Lett.* 86 (2001) 2685–2688. doi:10.1103/PhysRevLett.86.2685.  
URL <https://link.aps.org/doi/10.1103/PhysRevLett.86.2685>
- [21] R. I. Saye, J. A. Sethian, Multiscale modelling of evolving foams, *Journal of Computational Physics* 315 (2016) 273–301. doi:10.1016/j.jcp.2016.02.077.
- [22] J.-L. Auriault, L. Borne, R. Chambon, Dynamics of porous saturated media, checking of the generalized law of Darcy, *The Journal of the Acoustical Society of America* 77 (5) (1985) 1641–1650. doi:10.1121/1.391962.
- [23] D. L. Johnson, J. Koplik, R. Dashen, Theory of dynamic permeability and tortuosity in fluid-saturated porous media, *Journal of Fluid Mechanics* 176 (1987) 379–402. doi:10.1017/s0022112087000727.
- [24] D. Lafarge, P. Lemariner, J.-F. Allard, V. Tarnow, Dynamic compressibility of air in porous structures at audible frequencies, *The Journal of the Acoustical Society of America* 102 (4) (1997) 1995–2006. doi:10.1121/1.419690.
- [25] C. Lautensack, Fitting three-dimensional laguerre tessellations to foam structures, *Journal of Applied Statistics* 35 (9) (2008) 985–995. doi:10.1080/02664760802188112.
- [26] J. Koplik, On the effective medium theory of random linear networks, *Journal of Physics C: Solid State Physics* 14 (32) (1981) 4821. doi:10.1088/0022-3719/14/32/018.
- [27] V. Langlois, V. Trinh, C. Lusso, C. Perrot, X. Chateau, Y. Khidas, O. Pitois, Permeability of solid foam: Effect of pore connections, *Physical Review E* 97 (5) (2018) 053111. doi:10.1103/physreve.97.053111.
- [28] L. Cherel, G. Bonnet, J. Auriault, Locally periodic medium and homogenization of random media, *Archives of Mechanics* 40 (5-6) (1988) 529–542.
- [29] Y. Anguy, R. Erlich, C. Prince, V. Riggert, D. Bernard, The sample support problem for permeability assessment in sandstone reservoirs (1994).
- [30] S. R. du Roscoat, M. Decain, X. Thibault, C. Geindreau, J.-F. Bloch, Estimation of microstructural properties from synchrotron x-ray microtomography and determination of the rev in paper materials, *Acta Materialia* 55 (8) (2007) 2841–2850. doi:10.1016/j.actamat.2006.11.050.
- [31] J.-L. Auriault, C. Boutin, C. Geindreau, *Homogenization of Coupled Phenomena in Heterogenous Media*, Wiley-ISTE, 2009.
- [32] S. Wang, L. Qian, F. Xin, The synergistic flame-retardant behaviors of pentaerythritol phosphate and expandable graphite in rigid polyurethane foams, *Polymer Composites* 39 (2) (2018) 329–336.
- [33] J. Espadas-Escalante, F. Avilés, P. Gonzalez-Chi, A. Oliva, Thermal conductivity and flammability of multiwall carbon nanotube/polyurethane foam composites, *Journal of Cellular Plastics* 53 (2) (2017) 215–230. doi:10.1177/0021955X16644893.
- [34] W. Xi, L. Qian, Z. Huang, Y. Cao, L. Li, Continuous flame-retardant actions of two phosphate esters with expandable graphite in rigid polyurethane foams, *Polymer Degradation and Stability* 130 (2016) 97–102. doi:10.1016/j.polymdegradstab.2016.06.003.
- [35] T. Zhai, D. Li, G. Fei, H. Xia, Piezoresistive and compression resistance relaxation behavior of water blown carbon nanotube/polyurethane composite foam, *Composites Part A: Applied Science and Manufacturing* 72 (2015) 108–114. doi:10.1016/j.compositesa.2015.02.003.
- [36] J.-J. Cheng, B.-B. Shi, F.-B. Zhou, X.-Y. Chen, Effects of inorganic fillers on the flame-retardant and mechanical properties of rigid polyurethane foams, *Journal of Applied Polymer Science* 131 (10) (2014). doi:10.1002/app.40253.
- [37] L. Zhang, M. Zhang, Y. Zhou, L. Hu, The study of mechanical behavior and flame retardancy of castor oil phosphate-based rigid polyurethane foam composites containing expanded graphite and triethyl phosphate, *Polymer Degradation and Stability* 98 (12) (2013) 2784–2794. doi:10.1016/j.polymdegradstab.2013.10.015.
- [38] Y. Li, J. Zou, S. Zhou, Y. Chen, H. Zou, M. Liang, W. Luo, Effect of expandable graphite particle size on the flame retardant, mechanical, and thermal properties of water-blown semi-rigid polyurethane foam, *Journal of Applied Polymer Science* 131 (3) (2014). doi:10.1002/app.39885.
- [39] P. Acuña, Z. Li, M. Santiago-Calvo, F. Villafañe, M. Á. Rodríguez-Perez, D.-Y. Wang, Influence of the characteristics of expandable graphite on the morphology, thermal properties, fire behaviour and compression performance of a rigid polyurethane foam, *Polymers* 11 (1) (2019) 168. doi:10.3390/polym11010168.
- [40] N. Otsu, A threshold selection method from gray-level histograms, *IEEE transactions on systems, man, and cybernetics* 9 (1) (1979) 62–66. doi:10.1109/tsmc.1979.4310076.
- [41] A. Nistor, M. Toulec, A. Zubov, J. Kosek, Tomographic reconstruction and morphological analysis of rigid polyurethane foams, in: *Macromolecular Symposia*, Vol. 360, Wiley Online Library, 2016, pp. 87–95. doi:10.1002/masy.201500113.
- [42] J. Schindelin, I. Arganda-Carreras, E. Frise, V. Kaynig, M. Longair, T. Pietzsch, S. Preibisch, C. Rueden, S. Saalfeld, B. Schmid, et al., Fiji: an open-source platform for biological-image analysis, *Nature methods* 9 (7) (2012) 676.
- [43] D. Legland, I. Arganda-Carreras, P. Andrey, MorphoLibJ: integrated library and plugins for mathematical morphology with ImageJ, *Bioinformatics* 32 (22) (2016) 3532–3534. doi:10.1093/bioinformatics/btw413.
- [44] C. Redenbach, Microstructure models for cellular materials, *Computational Materials Science* 44 (4) (2009) 1397–1407. doi:10.1016/j.commatsci.2008.09.018.
- [45] A. Liebscher, C. Proppe, C. Redenbach, D. Schwarzer, Stochastic multiscale modeling of metal foams, *Procedia IUTAM* (6) (2013) 87–96. doi:10.1016/j.piutam.2013.01.010.
- [46] A. M. Kraynik, D. A. Reinelt, F. van Swol, Structure of random monodisperse foam, *Physical Review E* 67 (3) (2003) 031403. doi:10.1103/physreve.67.031403.
- [47] X.-Y. Meng, L. Ye, X.-G. Zhang, P.-M. Tang, J.-H. Tang, X. Ji, Z.-M. Li, Effects of expandable graphite and ammonium polyphosphate on the flame-retardant and mechanical properties of rigid polyurethane foams, *Journal of Applied Polymer Science* 114 (2) (2009) 853–863. doi:10.1002/app.30485.
- [48] A. Bensoussan, J.-L. Lions, G. Papanicolaou, *Asymptotic Analysis for Periodic Structures*, Studies in mathematics and its applications 5, North-Holland, 1978.
- [49] E. Sanchez-Palencia, *Non-Homogeneous Media and Vibration Theory*, 1st Edition, Lecture Notes in Physics N127, Springer-Verlag Berlin Heidelberg, 1980.
- [50] I. Malinetskaya, V. Mourzenko, J.-F. Thovert, P. Adler, Wave propagation through saturated porous media, *Physical Review E* 77 (6) (2008) 066302. doi:10.1103/physreve.77.066302.
- [51] J. Rubinstein, S. Torquato, Diffusion-controlled reactions: Mathematical formulation, variational principles, and rigorous bounds, *The Journal of chemical physics* 88 (10) (1988) 6372–6380. doi:10.1063/1.454474.
- [52] M. COMSOL, *Introduction to comsol multiphysics®*, COMSOL Multiphysics, Burlington, MA, accessed Feb 9 (1998) 2018.
- [53] J. Boulvert, T. Cavalieri, J. Costa-Baptista, L. Schwan, V. Romero-García, G. Gabard, E. R. Fotsing, A. Ross, J. Mardjono, J.-P. Groby, Optimally graded porous material for broadband perfect absorption of sound, *Journal of Applied Physics* 126 (17) (2019) 175101. doi:10.1063/1.5119715.
- [54] T. G. Zielinski, R. Venegas, C. Perrot, M. Cervenka, F. Chevillotte, K. Attenborough, Benchmarks for microstructure-based modelling of sound absorbing rigid-frame porous media, *Journal of Sound and Vibration* (2020) 115441doi:10.1016/j.jsv.2020.115441.
- [55] V. Langlois, C. T. Nguyen, F. Detrez, J. Guilleminot, C. Perrot, Permeability of polydisperse solid foams, *Phys. Rev. E* 105

- (2022) 015101. doi:10.1103/PhysRevE.105.015101.  
 URL <https://link.aps.org/doi/10.1103/PhysRevE.105.015101>
- [56] M. Biot, Theory of elastic waves in a fluid-saturated porous solid. 1. low frequency range, *J. Acoust. Soc. Am.* 28 (1956) 168–178. doi:<https://doi.org/10.1121/1.1908239>.
- [57] M. A. Biot, Theory of propagation of elastic waves in a fluid-saturated porous solid. ii. higher frequency range, *The Journal of the Acoustical Society of America* 28 (2) (1956) 179–191. doi:10.1121/1.1908241.
- [58] J. Allard, N. Atalla, *Propagation of Sound in Porous Media: Modelling Sound Absorbing Materials*, 2nd Edition, Wiley, 2009.
- [59] O. Dazel, F.-X. Bécot, L. Jaouen, Biot effects for sound absorbing double porosity materials, *Acta Acustica united with Acustica* 98 (4) (2012) 567–576. doi:10.3813/aaa.918538.
- [60] F.-X. Bécot, L. Jaouen, An alternative Biot’s formulation for dissipative porous media with skeleton deformation, *The Journal of the Acoustical Society of America* 134 (6) (2013) 4801–4807. doi:10.1121/1.4826175.
- [61] Y. Salissou, R. Panneton, Pressure/mass method to measure open porosity of porous solids, *Journal of Applied Physics* 101 (12) (2007) 124913. doi:10.1063/1.2749486.
- [62] E. Mariez, S. Sahraoui, J. Allard, Elastic constants of polyurethane foam’s skeleton for biot model, in: *Inter-Noise 96 (Noise control: the next 25 years, Liverpool, 30 July-2 August 1996)*, 1996, pp. 951–954.
- [63] C. Langlois, R. Panneton, N. Atalla, Polynomial relations for quasi-static mechanical characterization of isotropic poroelastic materials, *The Journal of the Acoustical Society of America* 110 (6) (2001) 3032–3040. doi:10.1121/1.1419091.
- [64] F. Chevillotte, F. Ronzio, C. Bertolini, M. T. Hoang, L. Dejaeger, A. Duval, P. Mordillat, et al., *Inter-Laboratory Characterization of Biot Parameters of Poro-Elastic Materials for Automotive Applications*, Tech. rep., SAE Technical Paper (2020). doi:10.4271/2020-01-1523.
- [65] O. Doutres, N. Atalla, K. Dong, Effect of the microstructure closed pore content on the acoustic behavior of polyurethane foams, *Journal of Applied Physics* 110 (6) (2011) 064901. doi:10.1063/1.3631021.
- [66] R. Panneton, X. Olny, Acoustical determination of the parameters governing viscous dissipation in porous media, *The Journal of the Acoustical Society of America* 119 (4) (2006) 2027–2040. doi:10.1121/1.2169923.
- [67] X. Olny, R. Panneton, Acoustical determination of the parameters governing thermal dissipation in porous media, *The Journal of the Acoustical Society of America* 123 (2) (2008) 814–824. doi:10.1121/1.2828066.
- [68] D. Pilon, R. Panneton, F. Sgard, Behavioral criterion quantifying the edge-constrained effects on foams in the standing wave tube, *The Journal of the Acoustical Society of America* 114 (4) (2003) 1980–1987. doi:10.1121/1.1598193.
- [69] P. Debergue, R. Panneton, N. Atalla, Boundary conditions for the weak formulation of the mixed (u, p) poroelasticity problem, *The Journal of the Acoustical Society of America* 106 (5) (1999) 2383–2390. doi:10.1121/1.428075.
- [70] N. Atalla, R. Panneton, P. Debergue, A mixed displacement-pressure formulation for poroelastic materials, *The Journal of the Acoustical Society of America* 104 (3) (1998) 1444–1452. doi:10.1121/1.424355.
- [71] J. Cuenca, P. Göransson, L. De Ryck, T. Lähivaara, Deterministic and statistical methods for the characterisation of poroelastic media from multi-observation sound absorption measurements, *Mechanical Systems and Signal Processing* 163 (2022) 108186. doi:10.1016/j.ymsp.2021.108186.
- [72] M. Firdaouss, J.-L. Guermond, D. Lafarge, Some remarks on the acoustic parameters of sharp-edged porous media, *International Journal of Engineering Science* 36 (9) (1998) 1035–1046. doi:10.1016/s0020-7225(98)00002-0.